

Turbulent transition of a flow from small to O(1) Rossby numbers

Jim Thomas^{1,2} and R. Vishnu³

¹ *International Centre for Theoretical Sciences, Tata Institute of Fundamental Research,
Bangalore, India*

² *Centre for Applicable Mathematics, Tata Institute of Fundamental Research, Bangalore, India*

³ *Fluid Mechanics Unit, Okinawa Institute of Science and Technology Graduate University,
Okinawa, Japan*

⁸ Corresponding author: Jim Thomas, jimthomas.edu@gmail.com

9 ABSTRACT: Oceanic flows are energetically dominated by low vertical modes. However, dis-
10 turbances in the form of atmospheric storms, eddy interactions with various forms of boundaries,
11 or spontaneous emission by coherent structures can generate weak high baroclinic modes. The
12 feedback of the low-energy high baroclinic modes on large scale energetically dominant low modes
13 may be weak or strong depending on the flow Rossby number. In this paper we study this interac-
14 tion using an idealized set up by constraining the flow dynamics to a high-energy barotropic mode
15 and a single low-energy high baroclinic mode. Our investigation points out that at low Rossby
16 numbers the barotropic flow organizes into large scale coherent vortices via an inverse energy
17 flux while the baroclinic flow accumulates predominantly in anticyclonic barotropic vortices. In
18 contrast, with increasing Rossby number, the baroclinic flow catalyzes a forward flux of barotropic
19 energy. The barotropic coherent vortices decrease in size and number, with a strong preference
20 for cyclonic coherent vortices at higher Rossby numbers. On partitioning the flow domain into
21 strain dominant and vorticity dominant regions based on the barotropic flow, we find that at higher
22 Rossby numbers, baroclinic flow accumulates in strain dominant regions, away from vortex cores.
23 Additionally, a major fraction of the forward energy flux of the flow takes place in strain dominant
24 regions. Overall, one of the key outcomes of this study is the finding that even a low-energy high
25 baroclinic flow can deplete and dissipate large scale coherent strcutures at $O(1)$ Rossby numbers.

26 **1. Introduction**

27 A significant fraction of oceanic mesoscale flow, with $O(100 \text{ km})$ lateral scales, is in geostrophic
28 and hydrostatic balance. These balance-constraints on the flow lead to an inverse energy flux,
29 organizing the balanced flow into large scale coherent vortices or eddies (Scott and Wang 2005,
30 Chelton et al. 2011). Since geostrophic energy on average gets transferred to larger scales, potential
31 mechanisms that can break these constraints, reverse the energy flux from inverse to forward, and
32 thereby enhance small scale dissipation of balanced flow are actively sought after. With the
33 mesoscale balanced flow being fed through instabilities of larger basin scale flow, identifying
34 potential mechanisms that can insinuate loss of balance and assist in small scale dissipation of
35 balanced energy is a crucial ingredient for closing the overall oceanic energy budget (Wunsch and
36 Stammer 1998, Ferrari and Wunsch 2010).

37 In addition to the balanced eddies, oceanic flows are rich in inertia-gravity waves generated by
38 atmospheric winds and gravitational tides. Contrary to the dynamics of the balanced flow, inertia-
39 gravity waves exhibit a forward energy flux and dissipate their energy at small viscous scales.
40 Furthermore, recent oceanic observational data-sets and realistically forced global scale ocean
41 model outputs reveal that depending on the geographic location and season, wave energy levels can
42 locally be comparable or stronger than balanced energy (Richman et al. 2012, Bühler et al. 2014,
43 Qiu et al. 2017, Savage and Coauthors 2017, Qiu et al. 2018, Tchilibou et al. 2018, Torres et al.
44 2018, Lien and Sanford 2019). These datasets have inspired a broad set of investigations aimed
45 at understanding how gravity waves interact with balanced flow and modify quasi-geostrophic
46 turbulent dynamics, specifically with an eye on deducing whether waves can form an energy sink
47 for balanced energy.

48 Dedicated idealized explorations using reduced asymptotic models, two-vertical-mode models,
49 and full Boussinesq equations (Gertz and Straub 2009, Xie and Vanneste 2015, Wagner and Young
50 2016, Taylor and Straub 2016, Rocha et al. 2018, Thomas and Yamada 2019, Thomas and Arun
51 2020, Xie 2020, Thomas and Daniel 2020, Taylor and Straub 2020, Thomas and Daniel 2021) have
52 revealed two key features of wave-balance exchanges in the small Rossby number regime. First,
53 there is no universal energy transfer direction between waves and balanced flows: depending on the
54 kind of wave field and relative energy levels of wave and balanced flow, waves can transfer energy
55 to or extract energy from balanced flow (see table 2 in Thomas and Daniel 2021). Second, waves

56 severely modify intrinsic balanced flow dynamics, such as the inverse energy flux and formation of
57 large scale coherent vortices, only when wave energy is significantly higher than balanced energy.
58 Specifically, waves irreversibly impact balanced flow in regimes where $E_G/E_W \lesssim Ro^2$, where E_G
59 and E_W denote balanced and waves' energies respectively and Ro is the Rossby number. These
60 findings point out that the balanced flow is extremely rugged in the small Rossby number regime
61 and can be perturbed only in the presence of high energy waves, irrespective of the kind of wave
62 field.

63 A different scenario for the breakdown of balanced flow and increased small scale dissipation
64 of balanced energy is when the flow Rossby number departs from asymptotically small values
65 and increases to $O(1)$ values. Such a scenario happens at oceanic submesoscales, these being
66 flows with lateral scales ranging from 0.1-10 km and timescales of the order of a day. A wide
67 range of in situ and satellite altimeter datasets along with high resolution simulations over the
68 past decade have identified the ubiquitous presence of energetic submesoscale flows in the world's
69 oceans, these submesoscale flows exhibiting significant departures from balanced flow dynamics
70 and quasi-geostrophic turbulence phenomenology (Lumpkin and Eliot 2010, Shcherbina et al.
71 2013, Xu and Fu 2011, Capet et al. 2008, Qiu et al. 2014, Brannigan et al. 2015, Thompson et al.
72 2016, Buckingham 2016, Poje et al. 2017, Barkan et al. 2017, Yu et al. 2019, Erickson et al.
73 2020). It is noteworthy that even straightforward numerical integration of ocean models, set in
74 boundary current regions and open ocean configurations, have found the generation of submesoscale
75 dynamics simply by increasing the resolution of the models (Capet et al. 2008, Brannigan et al.
76 2015). These ocean model outputs indicate increased small scale energy and shallower energy
77 spectra as spatial resolution is increased, resulting in a lack of numerical convergence of the ocean
78 model simulations with gradually increasing spatial resolution.

79 The widespread relevance of oceanic submesoscale flows and the limitations of ocean models
80 in fully resolving them makes it imperative to investigate various phenomenological aspects of
81 submesoscale flows in different configurations and understand how they depart from mesoscale
82 dynamics characterized by asymptotically small Rossby numbers. Quasi-geostrophic turbulence
83 and our understanding of mesoscale eddy dynamics has reached a mature level, thanks to a wide
84 range of idealized two-dimensional and three-dimensional studies that have explored intricate
85 details of turbulent balanced flow exchanges (McWilliams 1984, McWilliams 1989, Larichev and

86 Held 1995, Smith and Vallis 2001, Nadiga 2014). Similar dedicated exploratory attempts are key to
87 developing insights into the fluid dynamic aspects of O(1) Rossby number geophysical turbulence.
88 With these inspirations, in this paper we study a specific phenomenon: the changes accompanying
89 the turbulent dynamics of an idealized flow across different Rossby numbers, from low Rossby
90 number mesoscale regime to O(1) Rossby number submesoscale regime.

91 On examining energy content in vertical modes in the ocean, theoretical estimates, idealized
92 numerical simulations, and in situ observations reveal that most of the energy is contained in the
93 barotropic and the first few baroclinic modes (Fu and Flierl 1980; Wunsch 1997; Smith and Vallis
94 2001; Zhao et al. 2018). Despite this, external perturbations such as those generated by atmospheric
95 winds, eddies interacting with boundaries, or via spontaneous emission of high Rossby number
96 coherent structures can lead to the excitation of high baroclinic modes (Liang and Thurnherr 2012;
97 Alford et al. 2013; Gula et al. 2015; Clement et al. 2016; Alford et al. 2016; Gula et al. 2016).
98 While some specialized disturbances, such as extremely strong atmospheric storms (D'Asaro et al.
99 2011) can energize high baroclinic energy levels to a degree that they are comparable or stronger
100 than the energy content in the low modes, a wide variety of disturbances lead to configurations
101 where the low modes still remains the dominant flow component with high baroclinic energy levels
102 being relatively low. Consequently, constraining the flow to the barotropic and a high baroclinic
103 mode gives us an idealized two-vertical-mode model that can be used to investigate the energetic
104 interaction between a high-energy barotropic flow and a weak or low-energy high baroclinic mode.
105 Although the baroclinic flow remains energetically weak, the strength of the interaction may be
106 weak or strong depending on the Rossby number of the flow.

107 Flows with O(1) Rossby numbers are typically observed in the upper ocean in weakly sheared
108 eddies, or as eddies interact with topographic features (Boccaletti et al. 2007; Shcherbina et al.
109 2013; Buckingham 2016; Callies et al. 2015; Yu et al. 2019; Thompson et al. 2016; Gula et al.
110 2015, 2016). These commonly observed flows serve as an inspiration for our investigation in the
111 O(1) Rossby regime, although the extreme idealization of restricting the primitive equations to two
112 modes prevents a one-to-one correspondence between our set up and that of realistic oceanic flows.
113 Within our idealized set up we will explore how flow structures, energy flow pathways, and various
114 statistical quantities in physical space and spectral space change as Rossby number increases from
115 low to O(1) values.

¹¹⁶ The plan for the paper is as follows: we present the model and the parameter regimes in §2,
¹¹⁷ results in §3, and summarize our findings in §4.

¹¹⁸ **2. The two-vertical-mode model and numerical integrations**

¹¹⁹ The two-vertical-mode model used for our present study is obtained by projecting the f -
¹²⁰ plane primitive equations onto the barotropic and a single baroclinic mode imposing flat rigid
¹²¹ lid boundary conditions on top and bottom vertical boundaries and constant buoyancy fre-
¹²² quency. For example, the horizontal velocity field, \mathbf{v} , is expanded in vertical modes as:
¹²³ $\mathbf{v}(\mathbf{x}, z, t) = \mathbf{v}_T(\mathbf{x}, t) + \sqrt{2} \cos(n\pi z/H) \mathbf{v}_C(\mathbf{x}, t)$, where \mathbf{v}_T and \mathbf{v}_C denote the barotropic and the
¹²⁴ baroclinic horizontal velocity fields respectively, H is the depth of the ocean, and $\cos(n\pi z/H)$
¹²⁵ is the n^{th} baroclinic mode eigenfunction. Projecting the primitive equations on the barotropic
¹²⁶ and the n^{th} baroclinic mode gives a reduced two-dimensional model. The equations so obtained
¹²⁷ were then non-dimensionalized, choosing the inertial time scale, $1/f$ (where f is the constant
¹²⁸ rotation rate) as the time scale and the horizontal length scale L to be the length of the domain.
¹²⁹ An arbitrary velocity scale U was used to non-dimensionalize velocity fields and the geostrophic
¹³⁰ balance condition using the velocity scale U was used to obtain the scale for baroclinic pressure
¹³¹ (p_C). After non-dimensionalizing the reduced model, we obtain the equations:

$$\frac{\partial \zeta_T}{\partial t} + Ro \nabla \times (\mathbf{v}_T \cdot \nabla \mathbf{v}_T + \mathbf{v}_C \cdot \nabla \mathbf{v}_C + (\nabla \cdot \mathbf{v}_C) \mathbf{v}_C) = f_T - \nu \Delta^8 \zeta_T \quad (1a)$$

$$\frac{\partial \mathbf{v}_C}{\partial t} + \hat{\mathbf{z}} \times \mathbf{v}_C + Bu \nabla p_C + Ro (\mathbf{v}_T \cdot \nabla \mathbf{v}_C + \mathbf{v}_C \cdot \nabla \mathbf{v}_T) = \mathbf{f}_C - \nu \Delta^8 \mathbf{v}_C \quad (1b)$$

$$\frac{\partial p_C}{\partial t} + \nabla \cdot \mathbf{v}_C + Ro (\mathbf{v}_T \cdot \nabla p_C) = -\nu \Delta^8 p_C \quad (1c)$$

¹³² In the variables above, subscripts T and C indicate barotropic and baroclinic fields respectively,
¹³³ $Ro = U/fL$ represents the Rossby number, and $Bu = (NH/n\pi f L)^2$ is the Burger number. The
¹³⁴ gradient operator above is $\nabla = (\partial/\partial x, \partial/\partial y)$ and the curl operator shorthand used above is $\nabla \times \mathbf{v} =$
¹³⁵ $\nabla \times (u, v) = \partial v / \partial x - \partial u / \partial y$. The barotropic flow is divergence free and is entirely captured by the
¹³⁶ barotropic vorticity ζ_T , which is related to the barotropic streamfunction ψ_T via $\zeta_T = \nabla \times \mathbf{v}_T = \Delta \psi_T$.
¹³⁷ The terms f_T and \mathbf{f}_C in (1) denote barotropic and baroclinic forcing terms respectively while $\nu \Delta^8 \zeta_T$,
¹³⁸ $\nu \Delta^8 \mathbf{v}_C$, and $\nu \Delta^8 p_C$ are hyperdissipation terms removing energy reaching grid scale. In the absence

139 of forcing and dissipation, (1) conserves the total flow energy

$$\int_D \left(\frac{1}{2} \mathbf{v}_T^2 + \frac{1}{2} \mathbf{v}_C^2 + Bu \frac{1}{2} p_C^2 \right) d\mathbf{x} \quad (2)$$

140 where integration above is performed over the whole domain. The first term above is the barotropic
141 energy while the remaining two terms form the baroclinic energy.

142 At this point it is worth making a digression to note that the reduced model (1) was obtained
143 by projecting the primitive equations onto the barotropic and a high baroclinic mode assuming
144 rigid lid boundary conditions with vanishing vertical velocities on the top and bottom vertical
145 boundaries. As recent work has pointed out, such a projection needs to be modified in the presence
146 of realistic rough steep bottom topography (de La Lama et al. 2016; LaCasce 2017; LaCasce
147 and Groeskamp 2020). In realistic oceanographic scenarios with rough bathymetry, these studies
148 reveal that the dominant mode is the first baroclinic mode with vanishing bottom horizontal velocity.
149 Consequently, although for the present idealized study we use the two-vertical-mode in (1), the
150 model will need to significantly change to accommodate for more realistic oceanographic situations
151 involving surface intensified flows and rough bathymetry.

152 Returning to our study, for the governing equations (1) we chose a high baroclinic mode, i.e.
153 $n \gg 1$, making the Burger number a small parameter, $Bu \ll 1$. For the numerical integrations, we
154 specifically set $Bu = 0.1$. The results presented in this paper were obtained using 2/3rd dealiased
155 Fourier pseudospectral numerical integration of (1) in a doubly periodic domain with 576^2 grid
156 points. The forcing terms in (1a) and (1b) were used to generate turbulent flows in forced-dissipative
157 equilibrium. We chose a forcing scheme that maintains a constant energy level at low wavenumbers.
158 For the barotropic flow, we forced the low wavenumber band $k \in (0, k_f]$ with $k_f = 5$ such that the
159 total energy contained in the forced scales $(0, k_f]$ was enforced to be 1. For the baroclinic flow,
160 notice that in (1b) and (1c), in the absence of the nonlinear interaction terms, we are left with the
161 linear time evolving equations, whose solution consists of linear waves and a geostrophic balanced
162 mode. The $k = 0$ spatially homogeneous mode is the inertial oscillation mode. We chose the
163 baroclinic forcing such that the inertial oscillation mode was forced and maintained with energy
164 0.1. The forcing was therefore chosen such that the baroclinic flow is a small perturbation and
165 90% of the large scale flow energy was contained in the barotropic flow. We refer the reader to the
166 appendix for technical details of the forcing term.

167 The forcing scheme that maintains large scale energy of the flow to be constant has been used in
168 multiple turbulence studies in the past (Kaneda and Ishihara 2006, Donzis and Yeung 2010) and
169 has notable advantages. Specifically, the forcing scheme avoids the flow to evolve in a specific
170 way by enforcing a predetermined energy injection rate for the system. If there is an inverse flux
171 of energy, transferring flow energy to large scales, the energy at large scales tends to increase and
172 therefore to maintain same level of energy at large scales, forcing acts as an energy sink. On the
173 other hand, if the flow exhibits a forward energy flux depleting energy from large scales, the forcing
174 energizes large scales by acting as an energy source. Since the rate of energy transfer from large
175 to small scales at different Rossby numbers is not known apriori, we used the above forcing in our
176 study.

177 Our forcing scheme ensured that an energetically dominant barotropic flow was forced and
178 maintained at large scales, while low-energy spatially homogeneous inertial oscillations were
179 forced as a small perturbation. The inertial oscillations would interact with the barotropic flow and
180 generate spatial scales comparable to that of the barotropic flow; see detailed discussion of this
181 process in Thomas et al. 2017. For a comparison with our set up in the present study, the model
182 (1) was used by Thomas and Arun (2020) to examine interactions between inertial oscillations
183 and balanced flow in the small Rossby limit. Thomas and Arun specifically focused on the case
184 where baroclinic mode had significantly higher energy levels than the barotropic mode, a parameter
185 regime inspired by strong atmospheric winds exciting high energy inertial oscillations in the upper
186 ocean. In contrast, the present study explores the opposite regime, where the high vertical mode
187 baroclinic flow is a small perturbation to the barotropic flow – a common scenario in the ocean –
188 and the emphasis is on understanding how the low-energy baroclinic flow will modify the dynamics
189 of the barotropic flow as the Rossby number increases.

190 **3. Turbulent transition from small to O(1) Rossby numbers**

191 We used numerical solutions of (1) to study the flow dynamics across different Rossby numbers.
192 By forcing and maintaining low wavenumber energy as explained in the previous section, we
193 integrated (1) with different Ro values, changing Ro from 0.1 to 1 at increments of 0.01, providing
194 us with 91 flows characterized by a specific Ro value. Each flow, with a specific Ro , was evolved
195 for about thousand eddy turn over time scales and was checked for forced-dissipative equilibrium,

196 by ensuring that the barotropic and baroclinic energies, flow energy spectra, and all other statistical
197 quantities presented in this paper reached a steady state. Out of the 91 flows, 14 did not reach
198 equilibrium and were discarded. We therefore studied the transition from low to high Rossby
199 numbers using the remaining 77 equilibrated flows.

200 Although Ro is the parameter that we varied to generate different Rossby number flows and the
201 parameter explicitly appears in (1), we may unambiguously define the effective Rossby number
202 of each flow as $Ro_{eff} = Ro \zeta_{RMS}$, ζ_{RMS} being computed as the time-averaged root-mean-square
203 value of the nondimensional barotropic vorticity. (It is worth noting that based on our nondimen-
204 sionalization, the barotropic vorticity is nondimensionalized by U/L to obtain the nondimensional
205 vorticity ζ). Hereafter we will refer to each flow by its effective Rossby number, Ro_{eff} . Based
206 on this definition, for the lowest Rossby number flow, equilibrated by setting $Ro = 0.1$ in (1), we
207 obtained $Ro_{eff} = 0.29$ while for the highest Rossby number case where we set $Ro = 1$, we obtained
208 $Ro_{eff} = 3.41$.

209 Out of the 77 cases, figure 1 shows snapshots of barotropic vorticity ζ_T (left column) and baroclinic
210 speed $\sqrt{u_c^2 + v_c^2}$ (right column) for three flows with effective Rossby numbers: $Ro_1 = 0.29$,
211 $Ro_2 = 1.32$, and $Ro_3 = 3.41$. For the lowest Rossby number flow shown in figure 1(a), the
212 barotropic flow is seen to consist of large scale cyclonic (positive) and anticyclonic (negative)
213 coherent vortices, with like-signed vortices merging further to grow in size. On increasing Rossby
214 number, large scale vortices break up into smaller fragments that span the entire domain. This
215 feature can be seen in the intermediate Rossby number flow shown in figure 1(c). At the highest
216 Rossby number case shown in figure 1(e), the domain is rich with a lot of fine scale structures,
217 along with smaller scale vortices. Notice that the number and size of coherent vortices decreases
218 from top to bottom, as Rossby number is increased. The decrease in size of flow features can also
219 be seen in the right column of figure 1, showing baroclinic speed. At the lowest Rossby number, the
220 baroclinic flow has large scale structures, which breaks down into fine scale flow features spread
221 through out the domain as Rossby number is increased. The physical structures seen in figure 1 is
222 complemented by energy spectra of barotropic and baroclinic flow components shown in figure 2.
223 Concomitant with the generation of smaller scale features in the flow fields, the energy spectrum of
224 both barotropic and baroclinic modes becomes shallower with increasing Rossby number. Notably,

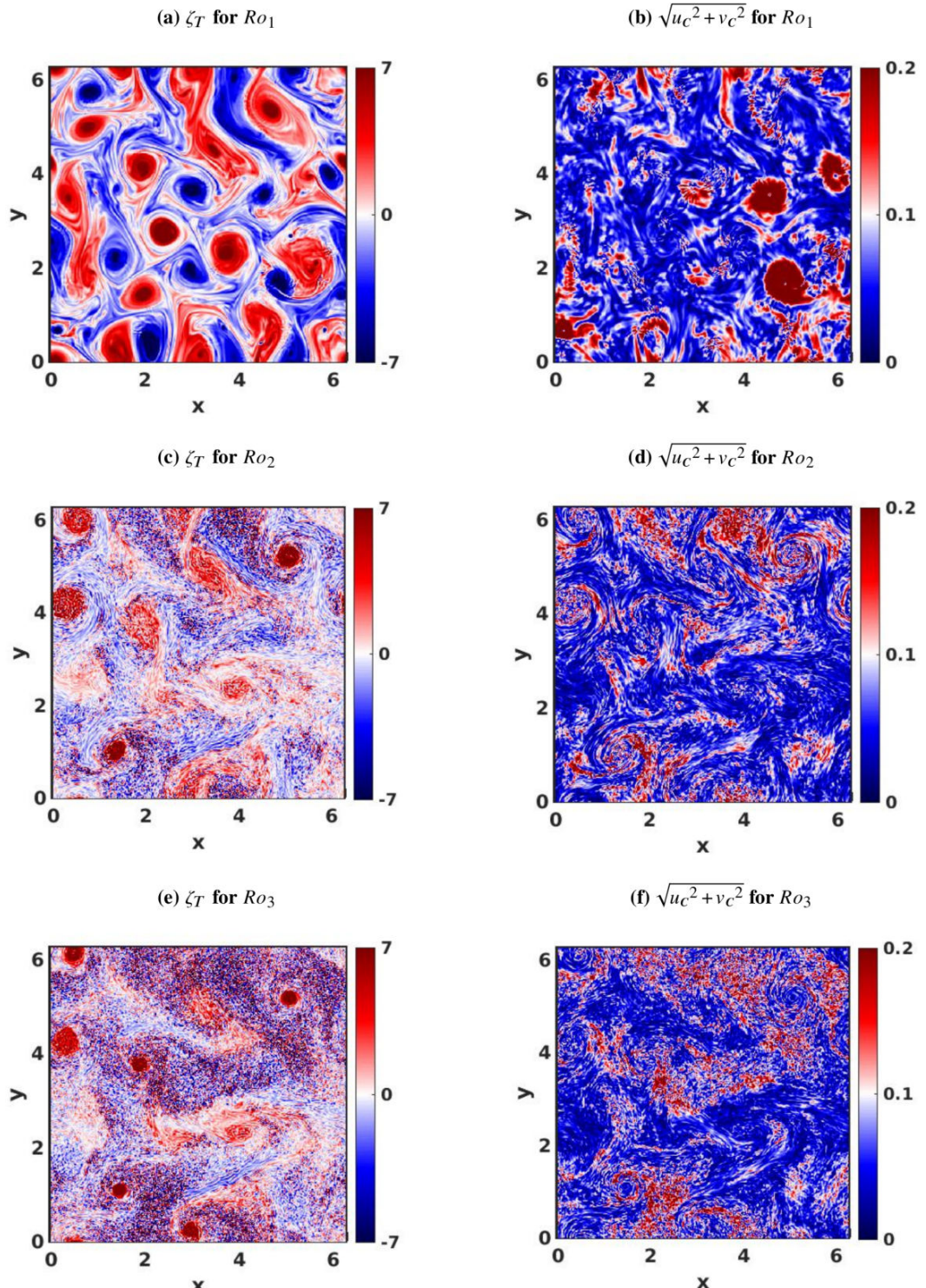


FIG. 1: Barotropic vorticity (left column) and baroclinic speed (right column) for three different Rossby numbers. Rossby number increases from top to bottom.

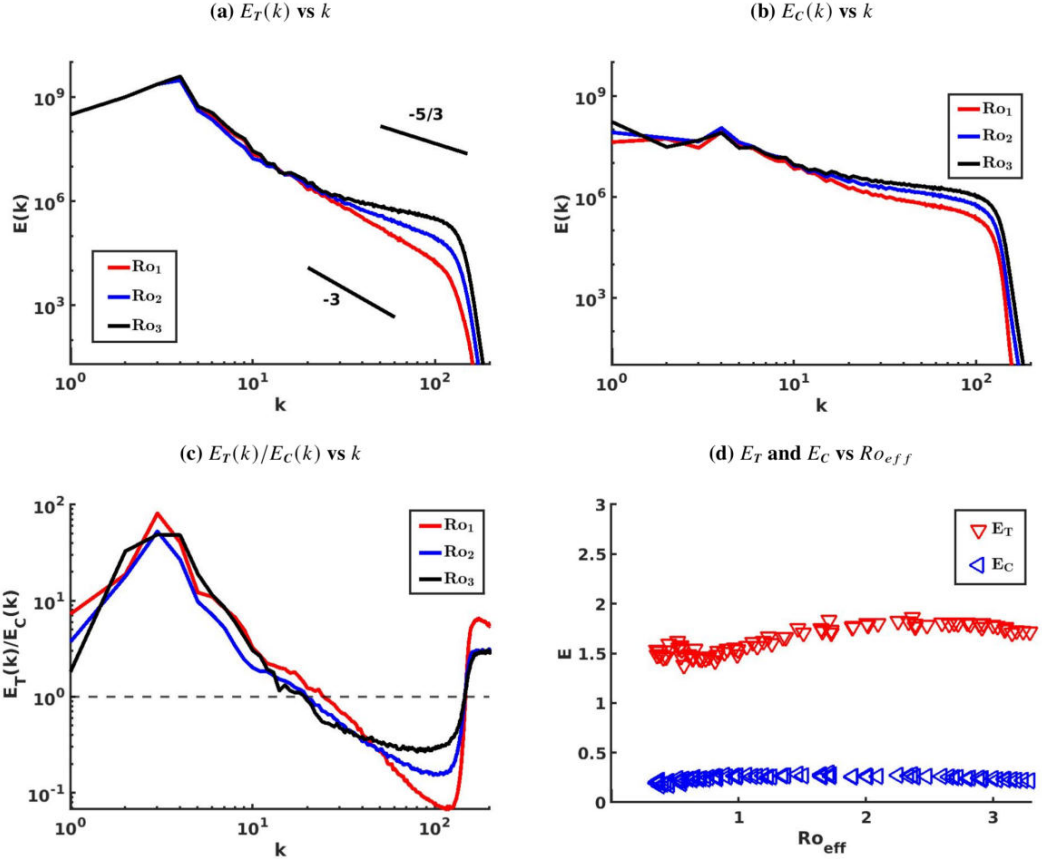


FIG. 2: Energy spectrum of (a) Barotropic flow and (b) Baroclinic flow for three different Rossby numbers. (c) Ratio of barotropic to baroclinic energy ratio across wavenumbers (d) Total barotropic (red) and total baroclinic (blue) energy as a function of Rossby number.

the barotropic spectrum shown in figure 2(a) has a slope close to -3 at low Rossby numbers, which changes to a shallow slope close to -5/3 at the highest Rossby number.

On comparing the energy spectrum of the barotropic and baroclinic fields in the top row of figure 2, it can be seen that the low wavenumber part of the energy spectrum, which contains most of the energy, has relatively lesser energy content for the baroclinic flow. This trend however reverses at smaller scales, as seen in figure 2(c) showing the barotropic to baroclinic energy ratio across wavenumbers: notice that although at large scales the ratio is much greater than 1, the ratio drops below 1 at smaller scales. The domain integrated energy content in the two flow fields is quantified in figure 2(d), which shows the barotropic and baroclinic energies of all the flows as a function of effective Rossby number. Since most of the energy is contained in large scales and since barotropic energy dominates over baroclinic energy at large scales, domain integrated energy

236 of the barotropic flow is about 8-10 times higher than that of the baroclinic flow. This feature
237 can also be qualitatively inferred from the physical structure plots shown in figure 1 – notice the
238 color bars of the figures on the left and right – the baroclinic flow structures are weaker than the
239 barotropic flow structures.

240 Recall that the forcing scheme we used ensured that the barotropic energy was maintained
241 at 1 at large scales and baroclinic energy was 0.1 in the inertial oscillation mode. The forced
242 inertial oscillation mode interacts with the barotropic flow and generates $k > 0$ wavenumbers in
243 the baroclinic flow. Therefore, although large scale barotropic energy was forced and maintained
244 to be much higher (90% of total energy) than the baroclinic energy, as the flows develops fine scale
245 features and transfers energy to smaller scales, this ratio could change. Nevertheless, figure 2(d)
246 shows that the baroclinic energy consistently an order of magnitude lower than barotropic energy,
247 implying that the barotropic flow remains the dominant flow component across Rossby numbers.
248 Despite being energetically weak compared to the barotropic flow, the low-energy baroclinic flow
249 is responsible for the significant changes in barotropic flow seen in the left column of figure 1.

250 To get a handle on the constituents of the energetically weak baroclinic flow, we decomposed
251 it into inertia-gravity waves and geostrophically balanced mode using the linear wave-balance
252 decomposition used in Thomas and Yamada (2019) (equations 2.12 there) and Thomas and Arun
253 (2020) (equations 8 and 9 there). Figure 3 shows the frequency spectrum of wave (blue) and
254 balanced (red) components. For the lowest Rossby number case shown in figure 3(a), a clear
255 separation can be seen between waves and balanced components. Notice how the balanced red
256 spectrum dominates at low frequencies while the blue wave spectrum overtakes the balanced
257 spectrum, around the inertial peak marked by a dashed vertical line, and remains the dominant
258 component at higher frequencies. In contrast, at the highest Rossby number case shown in figure
259 3(b) no distinct separation is seen between wave and balanced modes. Additionally, in the high
260 Rossby number case, the frequency spectrum of the balanced component is shallower and does not
261 decay as rapidly as in the low Rossby number case shown in figure 3(a). On further examining
262 the frequencies of specific wavenumbers of the wave field (figures omitted), the wave component
263 in the low Rossby regime was seen to have energy concentrated along frequencies dictated by
264 the dispersion relationship of inertia-gravity waves, $\omega(k) = \sqrt{1 + Bu k^2}$. In contrast, high Rossby
265 number wave component was seen to depart from the linear wave dispersion relationship, implying

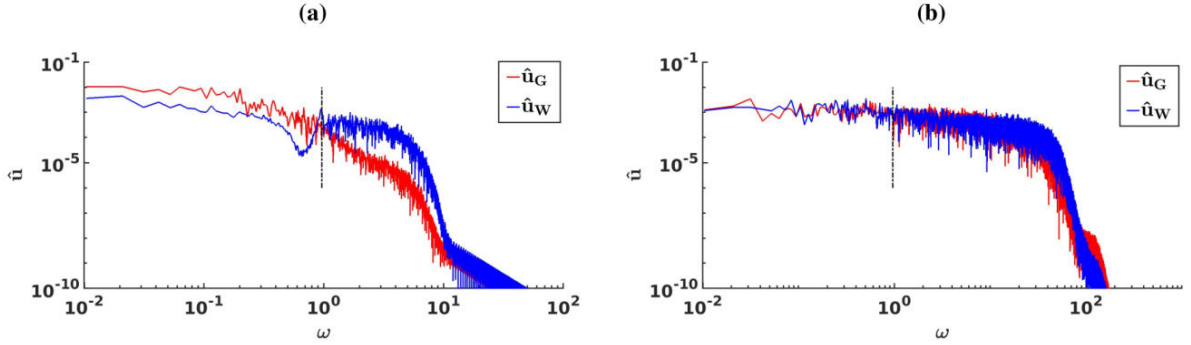


FIG. 3: Frequency spectrum of wave (blue) and balanced (red) fields for the lowest Ro_{eff} (a) and highest Ro_{eff} (b).

that even though the linear wave-balance decomposition provides us with a ‘wave’ component, that component do not correspond to linear inertia-gravity waves. These details point out that separating fast linear waves from slow balanced mode using the linear decomposition breaks down at high Rossby numbers. Overall, despite the baroclinic flow being energetically weak and its energy levels not changing appreciably on increasing Rossby number, the nature of the flow changes from being a separable mixture of fast waves and a slow balanced component at low Rossby numbers to a high frequency inseparable mixture of balance and waves in the $O(1)$ Rossby limit.

Returning to the flow features in physical space, oceanic observations of submesoscale dynamics typically find a pronounced cyclone-anticyclone asymmetry, with a dominance of cyclonic vorticity structures (Rudnick 2001, Shcherbina et al. 2013, Buckingham 2016). This feature is qualitatively seen in the left column of figure 1. The lowest Rossby number flow shown in figure 1(a) is composed of more or less the same number of cyclonic and anticyclonic vortices. In contrast, on closely examining figures 1(c) and 1(e), smaller scale cyclonic coherent vortices (red color) are seen to float in an incoherent soup of anticyclonic (blue color) vorticity regions. Although the size of cyclonic coherent vortices decreases with increasing Rossby number, cyclonic vortices remain rugged and persist while anticyclonic coherent vortices start disappearing with increasing Rossby number. Figure 4(a) quantifies the difference between cyclonic and anticyclonic vorticity structures based on the kurtosis. We divided the domain into positive and negative vorticity regions and computed the kurtosis for both positive and negative vorticity regions separately based on the

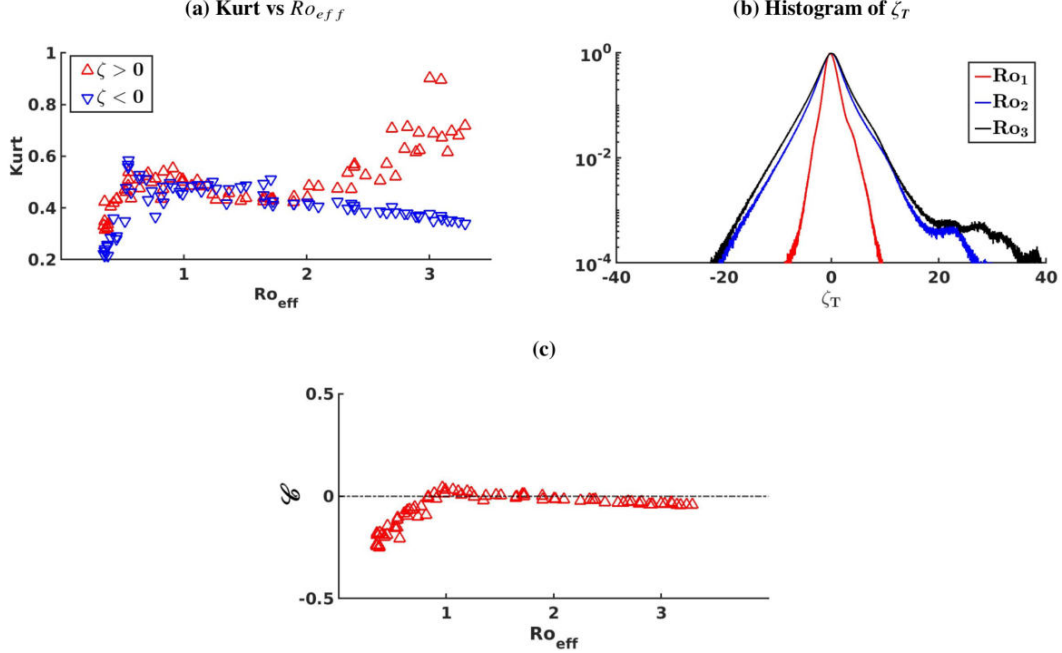


FIG. 4: (a) Kurtosis of cyclonic (red) and anti-cyclonic (blue) barotropic vorticity. (b) histogram of barotropic vorticity, ζ_T , for three different Rossby numbers. (c) Spatial correlation between barotropic and baroclinic flows based on equation (5).

285 expression (McWilliams 1984, Remmel and Smith 2009):

$$Kurt = \frac{\langle \zeta^4 \rangle}{(\langle \zeta^2 \rangle)^2} \quad (3)$$

286 where angle brackets above denote integrating over the domain. Kurtosis is in general higher
 287 for flows with coherent structures when compared with flows that have no coherent structures
 288 (McWilliams 1984). In figure 4(a), notice that on moving from low to high Rossby numbers, red
 289 markers keep moving above blue markers, indicating that cyclonic vortices have higher kurtosis
 290 and remain more coherent in comparison to anticyclonic vortices that have relatively lower kurtosis
 291 values and become incoherent. To further highlight the differences in positive-negative vorticity
 292 distributions on increasing Rossby number, figure 4(b) shows histograms of barotropic vorticity
 293 for three different Rossby numbers. To make the comparison between different Rossby number
 294 cases straightforward, we normalized the frequencies by the maximum frequency for each case,
 295 so that the highest frequency of the histogram is 1 for each case (notice that all three histograms
 296 meet at 1 on the y-axis). While the vorticity field is symmetric at the lowest Rossby number case

indicated by the red curve, the histograms become asymmetric at higher Rossby numbers. The skewness of the vorticity fields were seen to monotonically increase with Rossby number as 0.002, 0.06, and 0.15, with the vorticity field being least skewed at the lowest Rossby number case and maximum skewed at the highest Rossby number case. On examining figure 4(b) it can be inferred that for all three cases the high frequency low vorticity parts are more or less symmetric, implying that the weak background vorticity field, in which strong isolated vorticity structures float, exhibit less asymmetry. In contrast, the low frequency tails of the histograms in figure 4(b), exhibit a high level of asymmetry. It is seen that the extreme values of positive vorticity are almost double the extreme values of negative vorticity for the highest Rossby number case (black curve). These extreme values primarily correspond to spatially intermittent cyclonic coherent vortices seen in the left panel of figure 1. Therefore, with increasing Rossby number, cyclonic vortices remain coherent and take up higher vorticity values while anticyclonic vortices lose coherence and remain in the background with relatively lower extreme vorticity values.

Our analysis so far examined the properties of barotropic and baroclinic flows separately. To see the interconnection between the two flows, we will now examine the spatial correlation between barotropic and baroclinic fields. For this we computed the correlation between the pointwise baroclinic energy

$$e_c = \frac{\mathbf{v}_c^2}{2} + Bu \frac{p_c^2}{2} \quad (4)$$

and the barotropic vorticity ζ_T as:

$$\mathcal{C} = \frac{\langle \zeta_T e_c \rangle}{\sqrt{\langle \zeta_T^2 \rangle \langle e_c^2 \rangle}} \quad (5)$$

Above correlation coefficient is plotted in figure 4(c) as a function of Rossby number. Observe that at low Rossby numbers the correlation is negative, indicating that baroclinic energy has an affinity for anticyclonic vortices. This feature can be seen on comparing the physical structures in figures 1(a) and 1(b). Notice that the big red patches of baroclinic flow seen in figure 1(b) corresponds to anticyclonic (blue regions) in figure 1(a). As seen in figure 4(c), on increasing Rossby number the correlation coefficient moves closer to 0. At high Rossby numbers, as discussed above, anticyclonic vortices are destroyed, resulting in no clear correlation between anticyclonic barotropic vortices and baroclinic flow fields.

323 *a. Spectral fluxes of barotropic and baroclinic modes*

324 We will now examine energy transfers across scales for the barotropic and baroclinic fields.
 325 Applying Fourier transform to the governing equations (1) and manipulation resulting equations
 326 gives us energy equations for barotropic and baroclinic fields at each wavenumber k (see the
 327 procedure described in Thomas and Yamada 2019 for example). Summing the equations so
 328 obtained from the maximum resolved wavenumber k_{\max} to an arbitrary wavenumber k gives the
 329 energy flux equations for the barotropic and baroclinic flow as:

$$\frac{\partial \hat{E}_T(k,t)}{\partial t} = \underbrace{\Pi_{TTT}(k,t) + \Pi_{TCC}(k,t)}_{\Pi_T} + \hat{F}_T(k,t) - \hat{D}_T(k,t) \quad (6a)$$

$$\frac{\partial \hat{E}_C(k,t)}{\partial t} = \Pi_C(k,t) + \hat{F}_C(k,t) - \hat{D}_C(k,t) \quad (6b)$$

330 In the above equations, $\hat{E}_T(k,t)$ and $\hat{E}_C(k,t)$ are barotropic and baroclinic energies contained in
 331 the wavenumber band $[k, k_{\max}]$, while \hat{F}_T and \hat{F}_C are the forcing and \hat{D}_T and \hat{D}_C represent the
 332 dissipation contained in the same wavenumber band. The barotropic flux above is represented
 333 by Π_T while the baroclinic flux is denoted by Π_C . The barotropic flux is further divided into two
 334 parts: a part that is due to triadic barotropic interactions alone (Π_{TTT}) and a part that is due to joint
 335 barotropic-baroclinic triads (Π_{TCC}).

336 The flux terms given in (6) are shown in figure 5 for the same three Rossby numbers explored
 337 earlier. The barotropic flux Π_T shown in figure 5(a) reveals that the magnitude of the flux increases
 338 with increasing Rossby number. At low wavenumbers the flux is negative, while in the inertial
 339 range, $k \in [10, 100]$, it is positive. Positive barotropic flux in the inertial range implies that the
 340 barotropic energy is being transferred downscale, eventually getting dissipated. Furthermore, from
 341 figure 5(a) it is clear that the forward flux increases with Rossby number, with the flux being
 342 weakest in the inertial range for Ro_1 (red curve) and being the strongest for the highest Rossby
 343 number case Ro_3 (black curve). Consequently, on moving from top to bottom in the left column
 344 of figure 1, the generation of small scale features in the barotropic flow and shrinking in size of
 345 coherent vortices goes hand in hand with an increasingly strong forward flux of barotropic energy.

346 To explore the barotropic flux in more detail, the two components of the barotropic flux given in
 347 equation (6a), Π_{TTT} and Π_{TCC} are plotted in figures 5(b) and 5(c) respectively. Notice that although

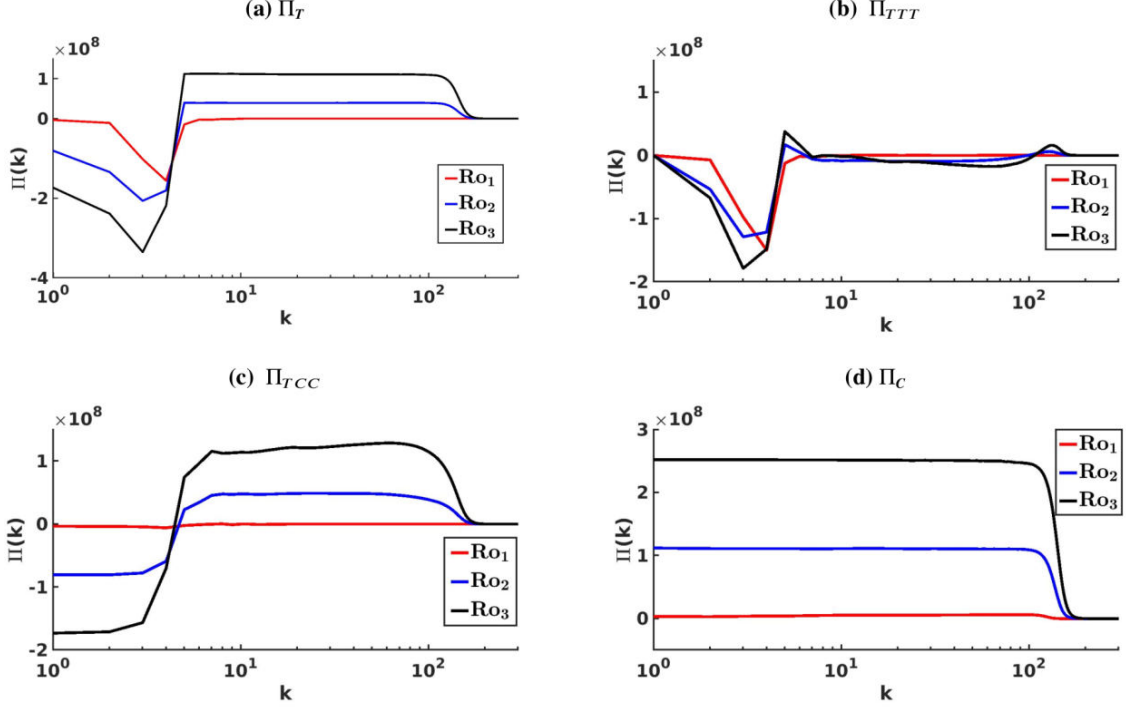


FIG. 5: Figure shows the barotropic flux, Π_T in panel (a), and its decomposition into two components, (b) Π_{TTT} and (c) Π_{TCC} . Baroclinic flux Π_C is shown in panel (d). Fluxes are shown for three different Rossby numbers. The red curves, corresponding to the lowest Rossby number, have the least flux while the black curves, corresponding to the highest Rossby number, have the largest flux.

the barotropic flux is constant and is represented by a straight line in the inertial range in figure 5(a), its constituents Π_{TTT} and Π_{TCC} exhibit a certain level of variability in the inertial range. Figure 5(b) shows that Π_{TTT} is negative, primarily at low wavenumbers, in addition to taking slightly negative values in the inertial range. Additionally, the Π_{TTT} flux component does not change appreciably with increasing Rossby number. The triadic barotropic interactions therefore assists in the upscale transfer of barotropic energy, with rates that are more or less comparable at different Rossby numbers. In contrast to the Π_{TTT} component, the Π_{TCC} flux component shown in figure 5(c) is positive through out the inertial range, with magnitude increasing with Rossby number. Π_{TCC} is negligible at the lowest Rossby number case (red curve) and reaches largest value at the highest Rossby number case (black curve). Since the Π_{TTT} component is insignificant in the inertial range, as seen in figure 5(b), the positive flux value in the inertial range seen in Π_T in figure 5(a) is entirely due to the Π_{TCC} flux component. Therefore, although the baroclinic energy is much less than the barotropic energy across different Rossby numbers, the baroclinic flow plays the dominant role in facilitating the forward energy flux of the barotropic flow.

362 In addition to the Π_{TCC} flux component being positive in the inertial range, as can be seen in
363 figure 5(c), Π_{TCC} is negative at low wavenumbers. Notice that Π_{TTT} goes to zero at the lowest
364 wavenumber in figure 5(b), while Π_{TCC} in figure 5(c) does not. This implies that the baroclinic flow,
365 in addition to catalyzing the forward flux of barotropic energy, also extracts some of the barotropic
366 energy. The energy transfer from barotropic to baroclinic mode is extremely small at low Rossby
367 number (notice that the red curve in figure 5(c) meets the y-axis at a value slightly below zero),
368 but increases monotonically with increasing Rossby number. Since in our numeral integrations we
369 forced the inertial oscillation mode of the baroclinic flow, the baroclinic flow is energized through
370 two separate sources: direct forcing and energy transfer from barotropic flow. Along the same
371 lines, the barotropic flow loses its energy by two means: energy loss to the baroclinic flow and
372 small scale dissipation at viscous scales. Since the energy transfer from barotropic to baroclinic
373 mode is a transfer from a low to a high vertical wavenumber mode, this transfer is essentially a
374 forward energy flux in the vertical wavenumber space restricted to two wavenumbers within our
375 idealized set up.

376 Complementary to the barotropic flux, figure 5(d) shows the baroclinic energy flux Π_c for three
377 different Rossby numbers. Π_c is seen to be positive and constant in the inertial range, with
378 magnitude increasing with Rossby number. The baroclinic flow, just like the barotropic flow,
379 undergoes a forward energy flux whose strength monotonically increases with Rossby number.
380 Additionally, as can be seen in figure 5(d), Π_c is positive at the lowest wavenumber, since as
381 explained earlier, the baroclinic flow is fed through direct forcing and energy transfer from the
382 barotropic flow. Therefore the baroclinic flow, fed through two different means, fluxes energy down
383 scale and dissipates at the viscous scales; the strength of the process increasing with increasing
384 Rossby number and being accompanied by the generation of finer scale features in the baroclinic
385 flow seen in the right column of figure 1.

386 *b. Flux distribution in physical space*

387 The spectral fluxes examined above clarifies energy transfer across scales for the flow. At higher
388 Rossby numbers both barotropic and baroclinic flow fluxes energy downscale and the forward
389 energy flux becomes stronger with increasing Rossby number. Despite spectral fluxes revealing
390 vital information regarding energy transfers across scales, it is still unclear where in physical space

391 the downscale energy transfers take place. For instance, gleaning from top to bottom of figure 1
 392 that shows shrinking barotropic coherent vortices and generation of finer scale features in the flow,
 393 it would be beneficial to understand the spatial structure of the forward energy flux with regard to
 394 the locations of the coherent vortices.

395 To identify locations where the forward energy flux of the flow dominate, we will now construct
 396 the energy flux equation in physical space. For this we applied a high-pass spatial filter on physical
 397 fields. We define filtered variable $\tilde{\psi}(\mathbf{x}, \tilde{k})$ as the streamfunction field restricted to scales greater
 398 than or equal to a cut-off scale $\tilde{L} = 2\pi/\tilde{k}$. $\tilde{\psi}$ is therefore obtained by a spectral filter that removes
 399 all components of the ψ that are larger than the cut off scale \tilde{L} or wavenumbers lower than \tilde{k} , i.e.
 400 $\tilde{\psi} = \mathcal{F}^{-1}(\hat{\psi}(k \geq \tilde{k}))$ where $\hat{\psi}$ is the Fourier transform of ψ , and \mathcal{F}^{-1} denotes the inverse Fourier
 401 transform. We apply the spectral filter to the governing equations (1) to get

$$\frac{\partial \tilde{\zeta}_T}{\partial t} + Ro \nabla \times \left(\widetilde{\mathbf{v}_T \cdot \nabla \mathbf{v}_T} + \widetilde{\mathbf{v}_c \cdot \nabla \mathbf{v}_c} + (\widetilde{\nabla \cdot \mathbf{v}_c}) \mathbf{v}_c \right) = \tilde{f}_T - \nu \Delta^8 \tilde{\zeta}_T \quad (7a)$$

$$\frac{\partial \tilde{\mathbf{v}}_c}{\partial t} + \hat{z} \times \tilde{\mathbf{v}}_c + Bu \nabla \tilde{p}_c + Ro \left(\widetilde{\mathbf{v}_T \cdot \nabla \mathbf{v}_c} + \widetilde{\mathbf{v}_c \cdot \nabla \mathbf{v}_T} \right) = \tilde{f}_c - \nu \Delta^8 \tilde{\mathbf{v}}_c \quad (7b)$$

$$\frac{\partial \tilde{p}_c}{\partial t} + \nabla \cdot \tilde{\mathbf{v}}_c + Ro \widetilde{\mathbf{v}_T \cdot \nabla p_c} = -\nu \Delta^8 \tilde{p}_c \quad (7c)$$

402 Above equations govern the evolution of flow variables constrained to scales smaller than \tilde{L} . To
 403 get energy equation of the flow for scales smaller than \tilde{L} , we multiply (7a) by $-\tilde{\psi}_T$, dot (7b) with
 404 $\tilde{\mathbf{v}}_c$, multiply (7c) with \tilde{p}_c and sum them up. After manipulating the terms by moving derivatives
 405 around, we get

$$\frac{\partial}{\partial t} \left(\frac{1}{2} \tilde{\mathbf{v}}_T^2 + \frac{1}{2} \tilde{\mathbf{v}}_c^2 + \frac{1}{2} Bu \tilde{p}_c^2 \right) = \nabla \cdot \mathbf{M}_1 + \nabla \times \mathbf{M}_2 + \nabla \cdot \mathbf{M}_3 + \tilde{\Pi}_T + \tilde{\Pi}_c + \tilde{F} - \tilde{D} \quad (8)$$

406 where

$$M_1 = -Bu \tilde{p}_c \tilde{\mathbf{v}}_c + \tilde{\psi}_T \nabla \frac{\partial \tilde{\psi}_T}{\partial t} \quad (9a)$$

$$M_2 = Ro \tilde{\psi}_T \left(\widetilde{\mathbf{v}_T \cdot \nabla \mathbf{v}_T} + \widetilde{\mathbf{v}_c \cdot \nabla \mathbf{v}_c} + (\nabla \cdot \widetilde{\mathbf{v}_c}) \mathbf{v}_c \right) \quad (9b)$$

$$M_3 = -Ro \left\{ \widetilde{v}_{Ti} (\widetilde{v_{Ti} \mathbf{v}_T} + \widetilde{v_{Ci} \mathbf{v}_C}) + \widetilde{v}_{Ci} (\widetilde{v_{Ti} \mathbf{v}_C} + \widetilde{v_{Ci} \mathbf{v}_T}) + Bu \widetilde{p}_c (\widetilde{p_c \mathbf{v}_T}) \right\} \quad (9c)$$

$$\tilde{\Pi}_T = Ro \frac{1}{2} \left(\frac{\partial \widetilde{v}_{Ti}}{\partial x_k} + \frac{\partial \widetilde{v}_{Tk}}{\partial x_i} \right) \widetilde{v_{Ti} v_{Tk}} \quad (9d)$$

$$\begin{aligned} \tilde{\Pi}_C &= Ro \frac{1}{2} \left(\frac{\partial \widetilde{v}_{Ti}}{\partial x_k} + \frac{\partial \widetilde{v}_{Tk}}{\partial x_i} \right) \widetilde{v_{Ci} v_{Ck}} + Ro \frac{1}{2} \left(\frac{\partial \widetilde{v}_{Ci}}{\partial x_k} + \frac{\partial \widetilde{v}_{Ck}}{\partial x_i} \right) (\widetilde{v_{Ti} v_{Ck}} + \widetilde{v_{Ci} v_{Tk}}) \\ &\quad + Ro \widetilde{v_{Ci}} \left(\widetilde{v_{Ti} \frac{\partial v_{Ck}}{\partial x_k}} \right) + Ro Bu (\widetilde{p_c v_{Tk}}) \frac{\partial \widetilde{p}_c}{\partial x_k} \end{aligned} \quad (9e)$$

407 For convenience we used the index notation in the expressions in (9), with v_i being the i^{th} component
 408 of the vector \mathbf{v} and repeated indices imply summation over that index.

409 In equation (8), the left hand side is the rate of change of flow energy contained in scales equal
 410 to and smaller than \tilde{L} and the right hand side contains terms responsible for the change, which
 411 are expanded in (9) (we refer readers not acquainted to equations like (8) to chapter 13 of Pope
 412 2000 for derivation of similar equations via filtering). Integrating (8) over the entire domain, the
 413 left hand side becomes the time rate of change of total energy contained in scales smaller than
 414 \tilde{L} , while the first three terms on the right hand side vanishes since they contain divergence and
 415 curl of vectors. Barring the contribution from the forcing and dissipation (expressed by the last
 416 two terms of (8)), the fourth and fifth terms on the right hand side of (8) – $\tilde{\Pi}_T$ and $\tilde{\Pi}_C$ – are the
 417 terms responsible for transferring energy across scales. It is important to keep in mind that (8)
 418 captures the rate of change of total flow energy. Consequently, $\tilde{\Pi}_T + \tilde{\Pi}_C$ in (8) represents the total
 419 flow energy flux in physical space, with $\tilde{\Pi}_T$ being flux contribution to the barotropic component
 420 alone while $\tilde{\Pi}_C$ is the flux contribution involving both barotropic and baroclinic modes. Equation
 421 (8) therefore is equivalent to the physical space representation of the sum of the barotropic and
 422 baroclinic energy flux equations given in (6). We examined $\tilde{\Pi}_T$ and $\tilde{\Pi}_C$ across the inertial range
 423 for different Rossby numbers. At all Rossby numbers, the energy flux involving barotropic modes
 424 alone, $\tilde{\Pi}_T$, was seen to be small in magnitude and negative in sign, implying that the barotropic
 425 modes by themselves were inducing a weak inverse energy flux of the flow. In contrast, the energy

426 flux involving baroclinic flow, $\tilde{\Pi}_c$, was seen to be positive in sign with its magnitude increasing
 427 monotonically with Rossby number. These inferences are qualitatively similar those inferred from
 428 spectral space transfers based on figure 5, i.e the barotropic triads induce a weak inverse energy
 429 flux while the flux involving the baroclinic term induces a forward energy flux whose strength
 430 increases monotonically with Rossby number. We will therefore take a closer look at the spatial
 431 structure of $\tilde{\Pi}_c$, this being the specific flux term that is responsible for the forward flux of the flow
 432 energy.

433 For the broad set of Rossby number flows discussed earlier, we examined $\tilde{\Pi}_c$ by choosing different
 434 filter wavenumber \tilde{k} (or filter scale \tilde{L}). A specific example of the spatial structure of the flux is
 435 given in figure 6(a), where $\tilde{\Pi}_c$ normalized by its spatially integrated value, $\langle \tilde{\Pi}_c \rangle$, is shown for the
 436 highest Rossby number flow, Ro_3 , with the filter wavenumber $\tilde{k} = 40$ (as can be seen from the
 437 energy spectra shown in figure 2, this corresponds to the middle of the inertial range, sufficiently
 438 far from forcing and dissipative scales). Observe in figure 6(a) that the flux is spatially intermittent
 439 and patchy, taking up both positive and negative values in physical space. Furthermore, as can be
 440 gleaned from the histogram of the flux shown in figure 6(b), extreme values of flux (positive and
 441 negative) have low frequency. Nevertheless from figure 6(b) it can be seen that the extreme positive
 442 values of flux are more frequent than extreme negative values of flux (notice that the black curve
 443 on the positive side goes up to 2 on the x-axis, while the curve falls off rapidly well before -2).
 444 This skewed flux with higher positive flux values in the domain results in the net flux integrated
 445 over the domain being positive, i.e. $\langle \tilde{\Pi}_c \rangle > 0$, indicating that the flow energy is transferred from
 446 large to small scales.

447 To get a handle on regions in physical space where the flow energy is fluxed downscale, we
 448 partitioned the flow domain into different regions based on the Okubo–Weiss criterion (Okubo
 449 1970, Weiss 1991), this decomposition being commonly used in the oceanography (Shcherbina
 450 et al. 2013, Chelton et al. 2007, Isern-Fontanet and Font 2006). For a flow velocity field (u, v) , if we
 451 define the normal strain rate as $\sigma_n = \partial u / \partial x - \partial v / \partial y$ and shear strain rate as $\sigma_s = \partial v / \partial x + \partial u / \partial y$,
 452 the total strain rate is $\sigma = \sqrt{\sigma_n^2 + \sigma_s^2}$. Based on flow vorticity $\zeta = \partial v / \partial x - \partial u / \partial y$, we may partition
 453 the flow domain as strain dominant regions, $\sigma > |\zeta|$, and vorticity dominant regions, $\sigma < |\zeta|$. Since
 454 the number of points that satisfied the exact equality $\sigma = |\zeta|$ were insignificantly small, we ignored
 455 such points to keep strict inequalities $\sigma > |\zeta|$ and $\sigma < |\zeta|$.

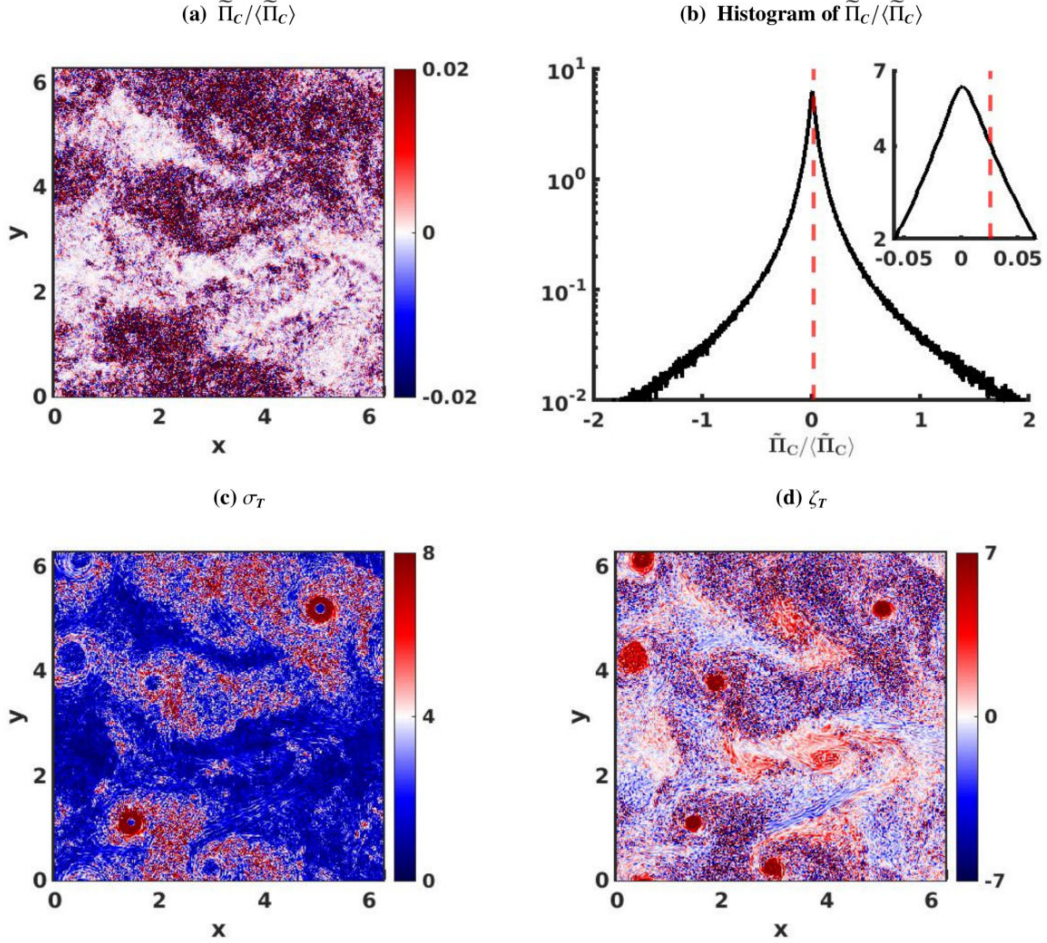


FIG. 6: (a) Spatial structure of normalized flux, $\tilde{\Pi}_c/\langle\tilde{\Pi}_c\rangle$. (b) Histogram of $\tilde{\Pi}_c/\langle\tilde{\Pi}_c\rangle$, corresponding to the flux shown in panel (a). The red dashed line indicates the mean of the normalized flux. The inset shows a smaller part of the histogram, highlighting the mean of the normalized flux. (c) Spatial structure of barotropic strain rate, σ_T . (d) Spatial structure of barotropic vorticity, ζ_T . Panel (d) is the same as figure 1(e), shown here for easier comparison between spatial structure of vorticity, strain rate, and flux.

For the highest Rossby number flow, figures 6(c) and 6(d) shows the spatial structure of total strain rate and vorticity of the barotropic flow respectively, computed at the same instant at which the flux in figure 6(a) was computed. On comparing the strain and vorticity fields shown in figures 6(c) and 6(d), it can be seen that strain takes up extremely large values in vortex peripheries, regions outside vortex cores. In contrast, vortex cores, seen with ‘holes’ in figure 6(c), are regions where strain is weak and vorticity dominates. Of course, as can be seen from figures 6(c) and 6(d), strain rate and vorticity field do take up sparse high values away from vortex structures, implying that there are small localized regions located away from vortices where strain rate dominates over vorticity and

vice versa. Nevertheless, on comparing pointwise strain rate and vorticity field at different times, above observation was seen to be a generic feature. A significant portion of strain dominant regions ($\sigma_T > |\zeta_T|$) are vortex peripheries while vortex cores are regions of vortex dominance ($\sigma_T < |\zeta_T|$).

To get a grip on the flux distribution in physical space, compare figures 6(a), 6(c), and 6(d). Notice that the flux takes up higher values in vortex peripheries, outside vortex cores, where strain rate dominates over vorticity. In fact, on closely staring at figure 6(a), the reader will notice ‘holes’ in the flux field, corresponding to physical locations of the vortex cores in figure 6(d), which are regions that appear as ‘holes’ in the strain rate shown in figure 6(c). To quantify flux distribution in physical space based on the strain-vorticity criterion, we spatially integrated $\tilde{\Pi}_c$ constrained to strain dominant regions ($\sigma_T > |\zeta_T|$) and vorticity dominant regions ($\sigma_T < |\zeta_T|$) and found that the former accounted for 61.5% of the flux while the latter constituted only 38.5% of the net flux. Therefore, the dominant fraction of the forward energy flux is based on strain dominant regions, away from vortex cores. Alternatively, vortex cores are regions of minimal net forward energy flux, the coherent structures being shielded from losing their energy to smaller dissipative scales.

The specific quantitative inferences made above are for the highest Rossby number case Ro_3 . Nevertheless, the qualitative features described above were robustly seen for other $O(1)$ Rossby number flows as well. On moving from asymptotically small to $O(1)$ Rossby numbers, the forward flux term $\tilde{\Pi}_c$ strengthens and a major fraction of the forward energy flux (generically more than 60%) takes place in strain dominated regions. Since the baroclinic flow plays a key role in the forward energy flux, via the $\tilde{\Pi}_c$ term, it is useful to examine the distribution of the pointwise baroclinic energy e_c with respect to the strain dominant and vorticity dominant regions. We therefore computed spatially integrated e_c (see expression in equation (4)) constrained on strain dominant and vorticity dominant regions. The results shown in figure 7(a) indicates that although at low Rossby numbers the contributions from the two regions are comparable, on increasing Rossby number, relatively higher level of baroclinic energy is associated with strain dominant regions in physical space. Recall that at low Rossby numbers the baroclinic flow has an affinity for anticyclonic barotropic vortices (as can be seen in the first row of figure 1). At $O(1)$ Rossby numbers, with anticyclonic barotropic vortices being destroyed, higher concentration of baroclinic flow shifts to barotropic strain dominant regions, outside cyclonic vortex cores (as can be seen in the last row of figure 1). On comparing spatial structure of small scale dissipation, similar

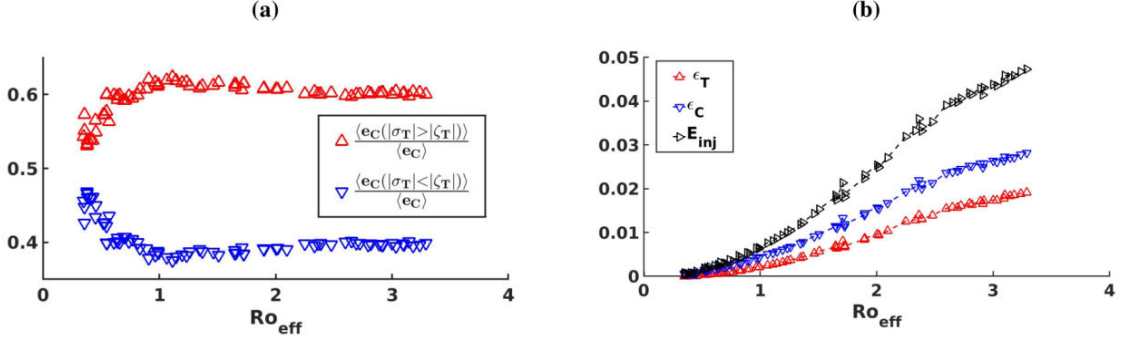


FIG. 7: (a) Fractional baroclinic energy in strain dominated (red curve) and vorticity dominated (blue curve) regions. (b) Barotropic dissipation (red curve), baroclinic dissipation (blue curve), and total energy injection rate (black curve).

to the spatial structure of flux, we found that the major fraction of flow dissipation was in strain dominant regions, with high dissipation values being observed in vortex peripheries. Therefore, with increasing Rossby number, the baroclinic flow migrates to regions outside vortex cores and strengthens the forward flux of flow energy, disintegrating peripheries of vortices and shrinking size of coherent vortices, as seen in the left column of figure 1, thereby enhancing small scale dissipation in those regions.

At this point we remind the reader that the flux equation (8) is for the total flow energy. Starting from the spatially filtered equations (7), it is straightforward to construct separate flux equations in physical space for the barotropic and baroclinic energy. We examined spatial structure of fluxes for the barotropic and baroclinic energy based on such equations (figures omitted) and found details similar to that mentioned above and gleaned from figure 6. The forward energy fluxes of both barotropic and baroclinic flow are generically dominant in regions where barotropic strain rate dominates over barotropic vorticity, these being regions where baroclinic energy levels are high.

Much of the detailed diagnosis described above requires high resolution spatio-temporal data that are difficult to obtain from typical oceanic observational campaigns. Nevertheless, Yang et al. (2017) is a recent work that compares properties of the flow in eddy core and eddy periphery regions with an eye on submesoscale dynamics. On exploring properties of multiple coherent eddies in South China Sea, they found that small scale features (shallower energy spectrum), forward energy flux, and small scale mixing was much more enhanced in eddy peripheries when compared with eddy core regions. While the sparse data sets they had access to prevented more detailed diagnosis, the key inferences of Yang et al. are qualitatively similar to our findings discussed above. That is,

515 the eddy peripheries are regions of higher concentration of energetic small scale flow structures,
516 stronger forward energy flux, and enhanced small scale dissipation when compared to eddy core
517 regions.

518 *c. Monotonic increase in small scale dissipation*

519 Returning to the spectral fluxes shown in figures 5(a) and 5(d), notice that the barotropic and
520 baroclinic forward flux in the inertial range increases with increasing Rossby number, suggesting
521 that higher amounts of energy is flowing through the system. To confirm this, figure 7(b) plots
522 barotropic dissipation, baroclinic dissipation, and total energy injection rate. The total energy
523 injection rate is the sum of energy injection rate into the barotropic and baroclinic modes and is
524 equal to the sum of barotropic and baroclinic dissipation in forced-dissipative equilibrium. As
525 mentioned earlier, the baroclinic flow is energized through direct external forcing and energy
526 transfer from the barotropic flow, due to which baroclinic dissipation (blue curve) is more than
527 barotropic dissipation (red curve) in figure 7(b). Observe the monotonic increase in all three
528 quantities with increasing Rossby number in figure 7(b). We remind the reader once again that our
529 forcing scheme does not impose a fixed rate of energy injection; energy at large scales are forced
530 and maintained and the system decides the energy flow rate through the system at different Rossby
531 numbers. Given this, it is interesting that larger and larger amount of energy flows through the
532 system with increasing Rossby number. More striking is this result in comparison to the result
533 seen in figure 2(d): although more and more energy flows through the system, the energy levels of
534 barotropic and baroclinic modes do not change appreciably. The increased drawing of energy into
535 the system is compensated by increased dissipation at small scales, resulting in more or less same
536 flow energy levels at different Rossby numbers.

537 **4. Summary and Perspectives**

538 Oceanic flows typically contain a major fraction of their energy in low vertical modes, while
539 various forms of external perturbations can generate low energy high baroclinic flow disturbances.
540 Although the high baroclinic disturbances may have low energy levels, the interaction between
541 the low and high modes may be weak or strong depending on the flow Rossby number. To
542 investigate energetic interactions and turbulent flow dynamics of an O(1) flow being capable of

543 sustaining large scale coherent structures with a weak high mode disturbance across different
544 Rossby numbers, we idealized the interaction problem by restricting the flow components to an
545 energetic barotropic mode and a single low-energy high baroclinic mode. Ignoring inertia-gravity
546 waves and other ageostrophic components, two-vertical-mode models have been extensively used
547 in the past in connection to geostrophic turbulence (Salmon 1978, Lariehev and Held 1995). As
548 an extension, recent work have used such reduced models to explore how inertia-gravity waves
549 modify geostrophic turbulence in the small Rossby number regime (Thomas and Yamada 2019,
550 Thomas and Arun 2020). Inspired by observations of energetic submesoscale flows with $O(1)$
551 Rossby numbers in the ocean, in the present work we explored the changes in flow structures and
552 energy flow pathways as Rossby number was gradually increased from asymptotically small to
553 $O(1)$ values.

554 To set up the flow at different Rossby numbers, we used a specialized set up where large scale
555 flow energy was forced and maintained to be a constant. The large scale barotropic flow, at
556 wavenumbers $k \leq 5$, was maintained to have unit energy while the spatially homogeneous inertial
557 oscillation mode of the baroclinic flow was forced and maintained at an energy 0.1. Using such
558 a set up ensured that we did not impose a fixed energy injection rate on the system; rather we let
559 the system choose the energy injection rate based on the energy flow rate through the system at
560 different Rossby numbers. We then numerically integrated the governing equations to generate 77
561 flows in forced-dissipative equilibrium, with Rossby number varying from asymptotically small
562 values to $O(1)$ values.

563 The inertial oscillation mode of the baroclinic flow, that was externally forced and maintained,
564 interacted with the barotropic flow and generated a spatially inhomogeneous baroclinic flow field
565 at all Rossby numbers. At low Rossby numbers, the barotropic flow exhibited an inverse energy
566 flux and organized itself into large scale coherent vortices while the baroclinic flow fluxed energy
567 downscale. The baroclinic flow was also seen to be concentrated in anticyclonic barotropic vortices.
568 The barotropic flow modified the dynamics of the baroclinic flow, along with a weak barotropic
569 to baroclinic energy transfer. In contrast, with increasing Rossby numbers, the barotropic and
570 baroclinic flow were rich with energetic small scale structures, shallower energy spectra, and
571 forward energy flux.

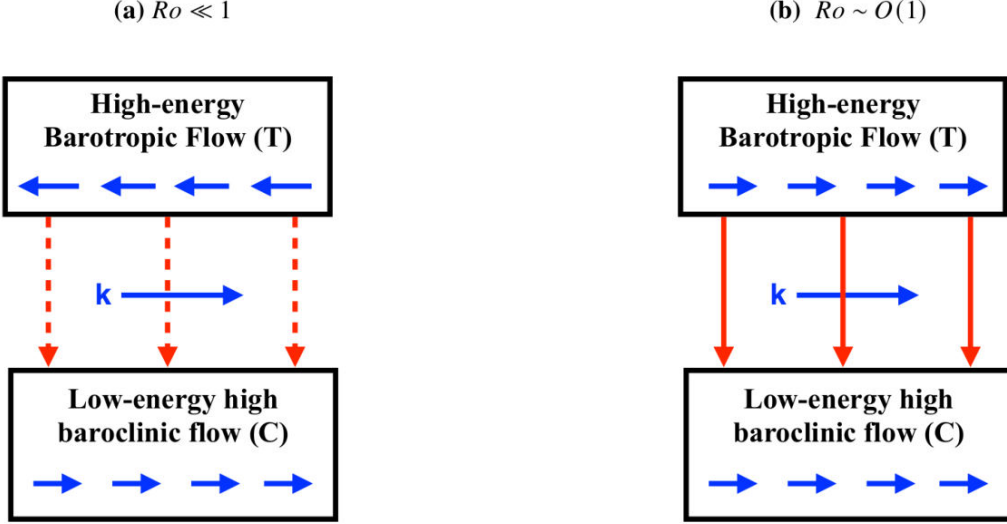


FIG. 8: Schematics of turbulent interactions between a high-energy barotropic flow (top box) and an energetically weak high baroclinic flow (bottom box). The blue arrows indicate energy transfer across scales, with wavenumber (k) increasing from left to right. The red arrows indicate energy transfer between modes. Panel (a) shows the energy transfers in the low Rossby number regime. The barotropic and baroclinic flows exhibit inverse and forward energy fluxes respectively, along with a weak energy transfer from barotropic to baroclinic mode as indicated by the dashed red arrows. Panel (b) shows the turbulent dynamics in the $O(1)$ Rossby number regime. The baroclinic flow extracts significantly more energy from the barotropic flow when compared to the low Rossby number case, as shown by the solid red arrows, undergoes a forward energy flux, and actively catalyzes a forward energy flux of the barotropic flow. Therefore, even though the baroclinic flow is an energetically weak flow component, in $O(1)$ Rossby number regimes it can insinuate a forward barotropic energy flux.

572 At low Rossby numbers, we observed symmetric distribution of cyclonic and anticyclonic vor-
 573 ticity structures of the barotropic flow. In contrast, $O(1)$ Rossby number flows were characterized
 574 by highly asymmetric barotropic vorticity distribution with a dominance of cyclonic vortices over
 575 anticyclonic ones. The barotropic coherent vortices at $O(1)$ Rossby numbers were seen to be fewer
 576 in number and smaller in size. Additionally, barotropic to baroclinic energy transfer was seen
 577 to increase monotonically with Rossby number. The $O(1)$ Rossby number flows were in general
 578 characterized by a forward energy flux for both barotropic and the baroclinic flow and the turbulent
 579 energy transfers in the two-vertical-mode system based on our present study is summarized in
 580 schematics shown in figure 8.

581 The forward energy flux of the flow was also seen to monotonically increase with increasing
 582 Rossby number. On partitioning the domain based on the barotropic flow field into vortex dominant
 583 regions, which were mostly regions inside vortex cores, and strain dominant regions, which

584 consisted of regions in the vortex peripheries, we found that the forward energy flux of the flow was
585 higher in strain dominant regions, away from vortex cores. Notably, these were also regions where
586 a major fraction of baroclinic flow was seen to be accumulated at high Rossby numbers. Therefore,
587 with increasing Rossby numbers, the forward energy flux of the flow strengthens, with higher net
588 flux in vortex peripheries, which goes hand-in-hand with shrinking size of coherent vortices, and
589 increased small scale dissipation.

590 As explained earlier, throughout out this work, across different Rossby numbers, we forced and
591 maintained large scale energy levels of the flow. Such a forcing scheme has no control over how
592 the total barotropic and baroclinic energy levels would change with different Rossby numbers.
593 Nevertheless, we observed that the barotropic and the baroclinic energy levels were not changing
594 appreciably with increasing Rossby number, ensuring that the major fraction of the flow energy was
595 associated with the barotropic flow, while the baroclinic flow was a small perturbation. The low-
596 energy baroclinic flow assisted in generating small scale barotropic flow features and facilitated the
597 forward flux of the flow energy, the intensity of which increased with increasing Rossby number.
598 Although multiple previous investigations based in idealized set ups, realistic ocean models, and
599 in situ observations have found the flow transition with a forward flux and increased small scale
600 dissipation at submesoscales (Barkan et al. 2017; Taylor and Straub 2016, 2020; Poje et al. 2017;
601 Naveira Garabato and Coauthors 2022), the low amount of unbalanced energy required to trigger
602 the transition is one of the highlights of this study. It is striking that this behavior is contrary to
603 the case in low Rossby numbers, where large scale coherent vortices remain rugged and persistent
604 unless unbalanced flow energy levels significantly exceed balanced energy (Thomas and Yamada
605 2019, Thomas and Arun 2020, Thomas and Daniel 2020, Thomas and Daniel 2021). In our present
606 investigation, even though the baroclinic flow remained a small perturbation to the total flow, the
607 baroclinic flow did more and more damage to the barotropic flow with increasing Rossby number.

608 To fully appreciate the significance of the last line above, it is worth comparing our results with
609 that of Dritschel and Viudez (2006), who integrated the Boussinesq equations enforcing balanced
610 constraints by filtering off unbalanced components of the flow during small time intervals of the
611 numerical integration (a procedure that they call ‘optimal balance’). By forcibly enforcing balance
612 constraints on the flow, thereby removing the unbalanced energy in the system, they observed that
613 the generic features of balanced flow holds even when Rossby number reaches O(1) values. In

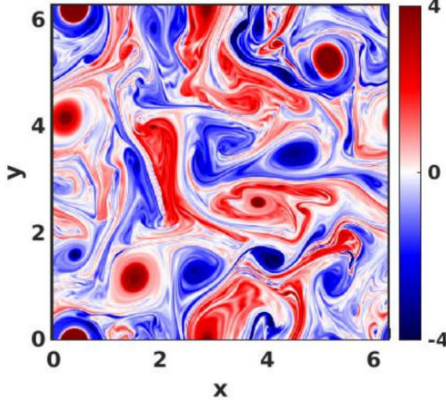


FIG. 9: Barotropic vorticity field with $Ro_{eff}=3.49$, obtained by integrating (1) with baroclinic flow forcibly filtered off along with time integration.

other words, balanced flow can be made to retain its features even at high Rossby numbers, if the unbalanced energy levels are enforced to be zero. To set up a similar experiment in our model, we integrated (1) with $Ro = 1$, forcibly setting the baroclinic flow to be zero after every few time steps of numerical integration. Figure 9 shows the barotropic vorticity field for such an integration with $Ro_{eff}=3.49$: observe the appearance of cyclonic and anticyclonic large scale coherent vortices. Of course, although our procedure of filtering off baroclinic flow along with time integration is a crude attempt to mimic the more rigorous optimal balance enforcing procedure of Dritschel and Viudez, a comparison between figure 9 and figure 1(e) drives the main message home: both these flows have similar $O(1)$ Rossby numbers, but the presence of a weak baroclinic flow makes a significant difference when compared to the situation with no baroclinic flow. In $O(1)$ Rossby number flows, even a small unbalanced energy can severely damage the large scale coherent flow structures.

A reader with interdisciplinary interests will find it intriguing to know that the result mentioned above has similarities with laminar to turbulence transition in pipe flows. Experimental investigations exploring pipe flows have found that the perturbation energy required to trigger transition from laminar to turbulent state decreases proportionally with increasing Reynolds number. Alternatively, the same perturbation magnitude can speed up the transition to turbulence and inflict more damage to the laminar flow at higher Reynolds numbers (Hof et al. 2003, Eckhardt et al. 2007). Although our work was not capturing a laminar to turbulent transition, the transition seen in the barotropic flow in the left column of figure 1 is a change from a well organised flow with most of its energy in large scale coherent vortices to a flow with relatively higher energy content

in incoherent small scale structures and with a strong forward energy flux. Therefore, although flows in pipe and the flows we investigated in this work in connection to geophysical turbulence in the ocean are poles apart, we may draw a qualitative analogy between the results in the two set ups. The same small unbalanced perturbation can cause more damage to the flow at higher Rossby numbers in geophysical turbulence and at higher Reynolds numbers in pipe flows.

We conclude by pointing out a specific ramification of the results of our study. Our goal in this paper was to examine how a low-energy high baroclinic mode, excited on top of an energetic barotropic mode, will affect the flow dynamics across different Rossby numbers. Intriguingly, we found that at O(1) Rossby numbers even low-energy high baroclinic flows can induce a forward energy flux and severely enhance dissipation of the flow energy. In the ocean, a wide range of perturbations can generate high baroclinic mode disturbances. Such unbalanced ageostrophic components, which includes inertial oscillations and near-inertial waves, are generated when geostrophic eddies interact with lateral boundaries, topographic features, or as a result of spontaneous emission by high Rossby number vortices and fronts (Liang and Thurnherr 2012, Alford et al. 2013, Clement et al. 2016). From the point of view of loss of balance, balanced coherent structures generating ageostrophic flow components is considered to be a mechanism by which the balanced flow loses energy, the energy being ‘lost’ from balanced flow to the newly excited unbalanced flow component. Despite such mechanisms being hypothesized to be an energy sink for balanced structures, the energy levels of the newly excited imbalance is usually small, compared to the mean or balanced energy. In connection to this, recall that our findings point out that high baroclinic perturbations in the O(1) Rossby number regime could irreversibly modify coherent vortices and enhance small scale dissipation. Therefore, in addition to balanced structures’ energy loss via the direct generation of unbalanced flow components, the newly generated unbalanced flow could feed back on the balanced structures and could potentially assist in the dissipation of the balanced structures that generated them. In other words, at O(1) Rossby numbers, newly excited unbalanced flow could do more damage to the structures that gave birth to them, than simply being a direct energy sink for the balanced coherent structures. We speculate that this feedback of unbalanced ageostrophic flow could play a role in dissipating balanced flow energy in localized high Rossby flow regions of the world’s oceans.

663 **5. Data availability**

664 The datasets used for this work can be downloaded from <https://zenodo.org/record/6673261>.

665 **APPENDIX**

666 Here we will describe the details of the forcing scheme used to enforce constant energy at large
 667 scales of the flow. The forcing scheme on the barotropic flow can be represented in spectral space
 668 as

$$\hat{\psi}_k^{(n+1)} = \hat{\psi}_k^{(n)} + a^{(n)} e^{i\theta_k^{(n)}} \quad (\text{A1})$$

669 where $a^{(n)} e^{i\theta_k^{(n)}}$ is the forcing term and $\hat{\psi}_k^{(n)}$ and $\hat{\psi}_k^{(n+1)}$ are the streamfunction fields before and
 670 after the forcing is implemented. At every iteration the phase $\theta_k^{(n)} \in [0, 2\pi)$ is randomly chosen.
 671 Our goal is to find the amplitude $a^{(n)} \in \mathbb{R}$ that will ensure constant energy at large scales. From
 672 (A1) we have

$$\left(k\hat{\psi}_k^{(n+1)*} \right) \left(k\hat{\psi}_k^{(n+1)} \right) = \left(k\hat{\psi}_k^{(n)*} + k a^{(n)} e^{-i\theta_k^{(n)}} \right) \left(k\hat{\psi}_k^{(n)} + k a^{(n)} e^{i\theta_k^{(n)}} \right) \quad (\text{A2a})$$

$$\Rightarrow k^2 |\hat{\psi}_k^{(n+1)}|^2 = k^2 |\hat{\psi}_k^{(n)}|^2 + k^2 a^{(n)2} + k^2 a^{(n)} \hat{\psi}_k^n e^{-i\theta_k^{(n)}} + k^2 a^{(n)} \hat{\psi}_k^{n*} e^{i\theta_k^{(n)}} \quad (\text{A2b})$$

673 Above $*$ denotes complex conjugate. We sum the above expression from $k > 0$ to $k = k_f$, since
 674 $k \in (0, k_f]$ is the forced band of wavenumbers, to get

$$\sum_{k \in (0, k_f]} k^2 |\hat{\psi}_k^{(n+1)}|^2 = \sum_{k \in (0, k_f]} k^2 |\hat{\psi}_k^{(n)}|^2 + a^{(n)2} \sum_{k \in (0, k_f]} k^2 + a^{(n)} \sum_{k \in (0, k_f]} k^2 \left(\hat{\psi}_k^{(n)} e^{-i\theta_k^{(n)}} + \hat{\psi}_k^{(n)*} e^{i\theta_k^{(n)}} \right) \quad (\text{A3})$$

675 The left hand side term above denotes the barotropic energy in the band $(0, k_f]$ after the forcing
 676 scheme is implemented and the first term on the right hand side above denotes the barotropic energy
 677 in the same wavenumber band before the forcing scheme is implemented. These two expressions
 678 should be equal to maintain constant total energy in the forced wavenumber band. Equating and

679 canceling these terms and further simplification of (A3) gives us

$$a^{(n)} = - \sum_{k \in (0, k_f]} k^2 \left(\hat{\psi}_k^{(n)} e^{-i\theta_k^{(n)}} + \hat{\psi}_k^{(n)*} e^{i\theta_k^{(n)}} \right) \Bigg/ \sum_{k \in (0, k_f]} k^2 \quad (\text{A4})$$

680 Above expression gives us the amplitude required in the forcing expression (A1) to maintain
681 constant barotropic energy in the forced wavenumber band $k \in (0, k_f]$. We used the same forcing
682 strategy as above to maintain constant energy in the inertial oscillation mode of the baroclinic flow.

683 References

- 684 Alford, M., J. MacKinnon, H. Simmons, and J. Nash, 2016: Near-inertial internal gravity waves
685 in the ocean. *Annu. Rev. Marine Science*, **8**, 95–123.
- 686 Alford, M. H., A. Y. Shcherbina, and M. C. Gregg, 2013: Observations of near-inertial internal
687 gravity waves radiating from a frontal jet. *J. Phys. Oceanogr.*, **43**, 1225–1239.
- 688 Barkan, R., K. B. Winters, and J. C. McWilliams, 2017: Stimulated imbalance and the enhancement
689 of eddy kinetic energy dissipation by internal waves. *J. Phys. Oceanogr.*, **47**, 181–198.
- 690 Boccaletti, G., R. Ferrari, and B. Fox-Kemper, 2007: Mixed layer instabilities and restratification.
691 *J. Phys. Oceanogr.*, **37**, 2228–2250.
- 692 Brannigan, L., D. P. Marshall, A. Naveira-Garabato, and N. A. J. G., 2015: The seasonal cycle of
693 submesoscale flows. *Ocean Model*, **92**, 69–84.
- 694 Buckingham, C. E. e. a., 2016: Seasonality of submesoscale flows in the ocean surface boundary
695 layer. *Geophys. Res. Lett.*, **43**, 2118–2126.
- 696 Bühler, O., J. Callies, and R. Ferrari, 2014: Wave-vortex decomposition of one-dimensional
697 ship-track data. *J. Fluid Mech.*, **756**, 1007–1026.
- 698 Callies, J., R. Ferrari, J. Klymak, and J. Gula, 2015: Seasonality in submesoscale turbulence. *Nat. Commun.*, **6**, 6862.
- 700 Capet, X., J. C. McWilliams, M. J. Molemaker, and A. F. Shchepetkin, 2008: Mesoscale to subme-
701 soscale transition in the California current system: flow structure, eddy flux, and observational
702 tests. *J. Phys. Oceanogr.*, **38**, 29–43.

- 703 Chelton, D. B., M. G. Schlax, and R. M. Samelson, 2011: Global observations of nonlinear
704 mesoscale eddies. *Prog. Oceanogr.*, **91**, 167–216.
- 705 Chelton, D. B., M. G. Schlax, R. M. Samelson, and R. A. de Szoeke, 2007: Global observations
706 of large oceanic eddies. *Geophys. Res. Lett.*, **34**, L15 606.
- 707 Clement, L., E. Frajka-Williams, K. L. Sheen, J. A. Brearley, and A. C. N. Garabato, 2016:
708 Generation of internal waves by eddies impinging on the western boundary of the north atlantic.
709 *J. Phys. Oceanogr.*, **46**, 1067–1079.
- 710 de La Lama, M. S., J. H. LaCasce, and H. K. Fuhr, 2016: The vertical structure of ocean eddies.
711 *Dyn. Stat. Clim. Sys.*, **dzw001**, 1–16.
- 712 Donzis, D. A., and P. K. Yeung, 2010: Resolution effects and scaling in numerical simulations of
713 passive scalar mixing in turbulence. *Physica D*, **239**, 1278.
- 714 Dritschel, D. G., and A. Viudez, 2006: The persistence of balance in geophysical flows. *J. Fluid
715 Mech.*, **570**, 365–383.
- 716 D’Asaro, E. A., L. Lee, C. and Rainville, R. Harcourt, and L. N. Thomas, 2011: Enhanced turbulence
717 and energy dissipation at ocean fronts. *Science*, **332**, 318–322.
- 718 Eckhardt, B., T. M. Schneider, B. Hof, and J. Westerweel, 2007: Turbulence transition in pipe flow.
719 *Annu. Rev. Fluid Mech.*, **39**, 447.
- 720 Erickson, Z. K., A. F. Thompson, J. Callies, X. Yu, A. Naveira Garabato, and P. Klein, 2020: The
721 vertical structure of open-ocean submesoscale variability during a full seasonal cycle. *J. Phys.
722 Oceanogr.*, **50**, 145–160.
- 723 Ferrari, R., and C. Wunsch, 2010: The distribution of eddy kinetic and potential energies in the
724 global ocean. *Tellus. Ser. A.*, **60**, 92–108.
- 725 Fu, L., and G. R. Flierl, 1980: Nonlinear energy and enstrophy transfers in a realistically stratified
726 ocean. *Dyn. Atmos. Oceans*, **4**, 219–246.
- 727 Gertz, A., and D. N. Straub, 2009: Near-inertial oscillations and the damping of midlatitude gyres:
728 A modelling study. *J. Phys. Oceanogr.*, **39**, 2338–2350.

- 729 Gula, J., M. J. Molemaker, and J. C. McWilliams, 2015: Topographic vorticity generation, sub-
730 mesoscale instability, and vortex street formation in the gulf stream. *Geophys. Res. Lett.*, **42**,
731 4054–4062.
- 732 Gula, J., M. J. Molemaker, and J. C. McWilliams, 2016: Topographic generation of submesoscale
733 centrifugal instability and energy dissipation. *Nat. communications*, **7**, 12 811.
- 734 Hof, B., A. Juel, and T. Mullin, 2003: Scaling of the turbulence transition threshold in a pipe.
735 *Phys. Rev. Lett.*, **91**, 244 502.
- 736 Isern-Fontanet, E., J. and Garcia-Ladona, and J. Font, 2006: Vortices of the mediterranean sea: An
737 altimetric perspective. *J. Phys. Oceanogr.*, **36**, 87–103.
- 738 Kaneda, Y., and T. Ishihara, 2006: High-resolution direct numerical simulation of turbulence. *J.*
739 *Turbul.*, **7**, 1–17.
- 740 LaCasce, J. H., 2017: The prevalence of oceanic surface modes. *Geo. Res. Lett.*, **44**, 11 097–11 105.
- 741 LaCasce, J. H., and S. Groeskamp, 2020: Baroclinic modes over rough bathymetry and the surface
742 deformation radius. *J. Phys. Oceano.*, **50**, 2835–2847.
- 743 Larichev, V. D., and I. M. Held, 1995: Eddy amplitudes and fluxes in a homogeneous model of
744 fully developed baroclinic instability. *J. Phys. Oceanogr.*, **25**, 2285–2297.
- 745 Liang, X., and A. M. Thurnherr, 2012: Eddy-modulated internal waves and mixing on a midocean
746 ridge. *J. Phys. Oceanogr.*, **42**, 1242–1248.
- 747 Lien, R.-C., and T. B. Sanford, 2019: Small-scale potential vorticity in the upper ocean thermocline.
748 *J. Phys. Oceanogr.*, **49**, 1845–1872.
- 749 Lumpkin, R., and S. Elipot, 2010: Surface drifter pair spreading in the north atlantic. *J. Geophys.*
750 *Res.*, **115**, C1207.
- 751 McWilliams, J. C., 1984: The emergence of isolated coherent vortices in turbulent flow. *J. Fluid*
752 *Mech.*, **146**, 21–43.
- 753 McWilliams, J. C., 1989: Statistical properties of decaying geostrophic turbulence. *J. Fluid Mech.*,
754 **198**, 199–230.

- 755 Nadiga, B. T., 2014: Nonlinear evolution of a baroclinic wave and imbalanced dissipation. *J. Fluid*
756 *Mech.*, **756**, 965–1006.
- 757 Naveira Garabato, A. C., and Coauthors, 2022: Kinetic energy transfers between mesoscale and
758 submesoscale motions in the open ocean’s upper layers. *J. Phys. Oceanogr.*, **52**, 75–97.
- 759 Okubo, A., 1970: Horizontal dispersion of floatable particles in the vicinity of velocity singularities
760 such as convergences. *Deep-Sea Res.*, **17**, 445–454.
- 761 Poje, A. C., T. M. Ozgokmen, D. J. Bogucki, and A. D. Kirwan, 2017: Evidence of a forward energy
762 cascade and kolmogorov self-similarity in submesoscale ocean surface drifter observations. *Phys*
763 *Fluids*, **29**, 020701.
- 764 Pope, S. B., 2000: *Turbulent Flows*. Cambridge University Press.
- 765 Qiu, B., S. Chen, P. Klein, H. Sasaki, and Y. Sasai, 2014: Seasonal mesoscale and submesoscale
766 eddy variability along the north pacific subtropical countercurrent. *J. Phys. Oceanogr.*, **44**,
767 3079–3098.
- 768 Qiu, B., S. Chen, P. Klein, J. Wang, H. Torres, L. Fu, and D. Menemenlis, 2018: Seasonality in
769 transition scale from balanced to unbalanced motions in the world ocean. *J. Phys. Oceanogr.*,
770 **48**, 591–605.
- 771 Qiu, B., T. Nakano, S. Chen, and P. Klein, 2017: Submesoscale transition from geostrophic flows
772 to internal waves in the northwestern pacific upper ocean. *Nat. Commun.*, **8**, 14 055.
- 773 Remmel, M., and L. Smith, 2009: New intermediate models for rotating shallow water and an
774 investigation of the preference for anticyclones. *J. Fluid Mech.*, **635**, 321–359.
- 775 Richman, J. G., B. K. Arbic, J. F. Shriver, E. J. Metzger, and A. J. Wallcraft, 2012: Inferring
776 dynamics from the wavenumber spectra of an eddying global ocean model with embedded tides.
777 *J. Geophys. Res.*, **117**, C12 012.
- 778 Rocha, C. B., G. L. Wagner, and W. R. Young, 2018: Stimulated generation-extraction of energy
779 from balanced flow by near-inertial waves. *J. Fluid Mech.*, **847**, 417–451.
- 780 Rudnick, D. L., 2001: On the skewness of vorticity in the upper ocean. *Geophys. Res. Lett.*, **28**,
781 2045–2048.

- 782 Salmon, R., 1978: *Lectures on Geophysical Fluid Dynamics*. Oxford University Press.
- 783 Savage, A., and Coauthors, 2017: Spectral decomposition of internal gravity wave sea surface
784 height in global models. *J. Geophys. Res. Oceans*, **122**, 7803–7821.
- 785 Scott, R. B., and F. M. Wang, 2005: Direct evidence of an oceanic inverse kinetic energy cascade
786 from satellite altimetry. *J. Phys. Oceanogr.*, **35**, 1650–1666.
- 787 Shcherbina, A. Y., E. A. D’Asaro, C. Lee, J. M. Klymak, M. J. Molemaker, and J. C. McWilliams,
788 2013: Statistics of vertical vorticity, divergence, and strain in a developed submesoscale turbu-
789 lence field. *Geophys. Res. Lett.*, **40**, 4706–11.
- 790 Smith, K. S., and G. K. Vallis, 2001: The scales and equilibration of midocean eddies: Freely
791 evolving flow. *J. Phys. Oceanogr.*, **31**, 554–571.
- 792 Taylor, S., and D. Straub, 2016: Forced near-inertial motion and dissipation of low-frequency
793 kinetic energy in a wind-driven channel flow. *J. Phys. Oceanogr.*, **46**, 79–93.
- 794 Taylor, S., and D. Straub, 2020: Effects of adding forced near-inertial motion to a wind-driven
795 channel flow. *J. Phys. Oceanogr.*, **50**, 2983–2996.
- 796 Tchilibou, M., L. Gourdeau, R. Morrow, G. Serazin, B. Djath, and F. Lyard, 2018: Spec-
797 tral signatures of the tropical pacific dynamics from model and altimetry: A focus on the
798 meso/submesoscale range. *Ocean Science*, **14**, 1283–1301.
- 799 Thomas, J., and S. Arun, 2020: Near-inertial waves and geostrophic turbulence. *Phys. Rev. Fluids*,
800 **5**, 014 801.
- 801 Thomas, J., and D. Daniel, 2020: Turbulent exchanges between near-inertial waves and balanced
802 flows. *J. Fluid Mech.*, **902**, A7.
- 803 Thomas, J., and D. Daniel, 2021: Forward flux and enhanced dissipation of geostrophic balanced
804 energy. *J. Fluid Mech.*, **911**, A60.
- 805 Thomas, J., K. Smith, and O. Bühler, 2017: Near-inertial wave dispersion by geostrophic flows.
806 *J. Fluid Mech.*, **817**, 406–438.
- 807 Thomas, J., and R. Yamada, 2019: Geophysical turbulence dominated by inertia-gravity waves. *J.*
808 *Fluid Mech.*, **875**, 71–100.

- 809 Thompson, A. F., A. Lazar, C. E. Buckingham, A. C. Naveira Garabato, G. M. Damerell, and
810 K. J. Heywood, 2016: Open-ocean submesoscale motions: A full seasonal cycle of mixed layer
811 instabilities from gliders. *J. Phys. Oceanogr.*, **46**, 1285–1307.
- 812 Torres, H. S., P. Klein, D. Menemenlis, B. Qiu, Z. Su, J. Wang, S. Chen, and L.-L. Fu, 2018:
813 Partitioning ocean motions into balanced motions and internal gravity waves: A modeling study
814 in anticipation of future space missions. *J. Geophys. Res. Oceans*, **123**, 8084–8105.
- 815 Wagner, G. L., and W. R. Young, 2016: A three-component model for the coupled evolution
816 of near-inertial waves, quasi-geostrophic flow and the near-inertial second harmonic. *J. Fluid
817 Mech.*, **802**, 806–837.
- 818 Weiss, J., 1991: The dynamics of enstrophy transfer in two-dimensional hydrodynamics. *Physica
819 D*, **48**, 273–294.
- 820 Wunsch, C., 1997: The vertical partition of oceanic horizontal kinetic energy and the spectrum of
821 global variability. *J. Phys. Oceanogr.*, **27**, 1770–1794.
- 822 Wunsch, C., and D. Stammer, 1998: Satellite altimetry, the marine geoid and the oceanic general
823 circulation. *Annu. Rev. Earth Planet. Sci.*, **26**, 219–254.
- 824 Xie, J., and J. Vanneste, 2015: A generalised-lagrangian-mean model of the interactions between
825 near-inertial waves and mean flow. *J. Fluid Mech.*, **774**, 143–169.
- 826 Xie, J.-H., 2020: Downscale transfer of quasigeostrophic energy catalyzed by near-inertial waves.
827 *J. Fluid Mech.*, **904**, A40.
- 828 Xu, Y., and L.-L. Fu, 2011: Global variability of the wavenumber spectrum of oceanic mesoscale
829 turbulence. *J. Phys. Oceanogr.*, **41**, 802–809.
- 830 Yang, Q., W. Zhao, X. Liang, J. Dong, and J. Tian, 2017: Elevated mixing in the periphery of
831 mesoscale eddies in the south china sea. *J. Phys. Oceanogr.*, **47**, 895–907.
- 832 Yu, X., A. C. Naveira Garabato, A. P. Martin, C. E. Buckingham, L. Brannigan, and Z. Su, 2019:
833 An annual cycle of submesoscale vertical flow and restratification in the upper ocean. *J. Phys.
834 Oceanogr.*, **46**, 1439–1461.

- 835 Zhao, M., M.-L. Timmermans, R. Krishfield, and G. Manucharyan, 2018: Partitioning of kinetic
836 energy in the arctic ocean's beaufort gyre. *J. Geophys. Res. Ocea.*, **123**, 4806–4819.